Article

Phase Field Simulation of Al-Fe-Mn-Si Quaternary Eutectic Solidification

Kimiya NouraniNiaki [1,*], Murali Uddagiri [2,3], Daysianne Isidorio [2], Oleg Shchyglo [2,3] and Ingo Steinbach [2,3]

[1] Institute for Applied Materials-Microstructure Modelling and Simulation (IAM-MMS), Karlsruhe Institute of Technology (KIT), Straße am Forum 7, 76131 Karlsruhe, Germany
[2] Interdisciplinary Centre for Advanced Materials Simulation, Ruhr Universität Bochum, Universität Street 150, 44801 Bochum, Germany; ingo.steinbach@rub.de (I.S.)
[3] OpenPhase Solutions GmbH, Universitäts Street 136, 44799 Bochum, Germany
* Correspondence: kimiya.niaki@kit.edu

Abstract: This study investigates the eutectic equilibrium phases in a multicomponent system through 3-D multi-phase-field simulations. Emphasizing the directional solidification process, the work examines the growth dynamics of intermetallic phase $Al_{13}Fe_4$, a lamellar structure (FCC-A1), and a quaternary phase beta-AlMnSi from the liquid that is solidified at a specific temperature. The eutectic transformation, described by the four phase reaction $L \rightarrow Al_{13}Fe_4 + FCC\text{-}A1 + beta\text{-}AlMnSi$, is analyzed to develop a microstructure selection map. This map correlates stable growth modes with initial system composition and lamellar spacing. The results provide detailed insights into the segregation behaviour of alloying elements and their influence on transformation kinetics, enhancing the understanding of eutectic microstructure evolution in complex alloy systems.

Keywords: aluminum; solidification; intermetallic; quaternary; multi-phase-field

1. Introduction

Aluminum alloys are extensively utilized in automotive, aerospace, and transportation industries due to their superior mechanical properties and sustainability potential. The increasing global emphasis on environmental sustainability and the rising demand for aluminum alloys can be effectively addressed by incorporating recycled aluminum alloys. This approach not only reduces production costs but also decreases energy consumption.

Among commonly used aluminum alloys, the 3000 series is notable for its lightweight nature, high mechanical strength, and excellent formability [1]. Key alloying elements such as Fe, Mn, and Si play critical roles in enhancing these properties: Fe prevents mold sticking during die casting [2], Si improves liquid phase fluidity [3,4], and Mn stabilizes intermetallic phases [5,6], thereby improving mechanical properties. However, choosing the right composition of these elements is crucial, as exceeding their weight fractions can lead to the formation of brittle intermetallic compounds [7], adversely affecting mechanical performance. Therefore, effective control of phase formation is essential to optimize the mechanical properties of aluminum alloys during design and manufacturing [8–11].

To explore the large compositional space of multicomponent alloys, computational methods are employed to predict phase behavior under solidification and equilibrium conditions. Thermodynamic models are valuable tools for designing aluminum alloys [12,13]. The CALPHAD approach is widely used for material design and process optimization of aluminum alloys [1,14]. The strength of the CALPHAD method lies in its ability to

use self-consistent parameters to predict thermodynamic behavior in multicomponent systems [8,15].

Phase field modeling is another computational approach that simulates complex systems, such as solidification [16], segregation [17–19], and grain growth [20], using thermodynamically grounded partial differential equations [21]. Accurately predicting changes in precipitate morphology, size, volume fraction, and spatial distribution during heat treatment is critical for understanding precipitate hardening effects. Meso-scale simulations, such as those for Al_2Cu precipitates, provide insights into these processes [22]. The phase field method, particularly with diffuse interface approaches, simplifies modeling by eliminating the need for explicit interface tracking [21].

Understanding and designing aluminum alloys through thermodynamic models is enhanced by numerical simulations. These models allow for the analysis of various factors influencing microstructural evolution [22–27]. However, evidence of distinct quaternary phases in aluminum alloys is limited. For instance, the α-AlMnSi phase extends significantly into the quaternary system, approaching the ternary Al-Fe-Si system, yet no stable quaternary phase exists in the aluminum-rich corner of the Al-Fe-Mn-Si system [28]. Combining computational thermodynamics with multi-phase-field models enables a detailed analysis of phase distributions in multicomponent systems. According to Warmuzek [29], rod-shaped FCC-A1 morphology can form through eutectic transformation involving two key reactions: However, experimental data on quaternary phases in multicomponent aluminum alloys remains scarce.

Furthermore, $Al_{13}Fe_4$ is an important intermetallic phase in the Al-Fe-Mn-Si system because of its influence on the microstructure and properties of Al-based alloys. This phase is the only equilibrium phase forming in the Al-rich corner of the Al–Fe–Si system and it forms during solidification as part of eutectic reaction. This phase is especially common in recycled aluminum alloys, where iron tends to accumulate due to its low solubility in aluminum. As reported in Quan Li et al. [7], the $Al_{13}Fe_4$ intermetallic phase negatively impacts the mechanical properties of recycled aluminum alloys with high iron content by acting as a stress concentrator, reducing ductility and corrosion resistance [30]. Therefore, understanding the formation, morphology, and interactions of this phase with other intermetallics is essential for designing alloys that mitigate its detrimental effects [31]. Such research contributes to improving the structural performance, recyclability, and mechanical and corrosion-resistant properties of aluminum alloys [32].

The objective of this study is twofold: first, to develop a microstructural selection map of eutectic solid phases formed via key reactions leading to the emergence of the quaternary phase beta-AlMnSi; and second, to employ the phase field method to characterize the quaternary phase both qualitatively and quantitatively. This study focuses on the lamellar structure of FCC-A1, intermetallic precipitation, microstructural evolution, and the spatial distribution of beta-AlMnSi as the quaternary phase. These investigations, conducted through multi-phase-field simulations, aim to provide a comprehensive understanding of the mechanisms governing microstructure formation in complex eutectic systems.

2. Literature Review of Thermodynamic Modeling of Aluminum Systems

The equilibrium phase diagram of the quaternary Al-Fe-Mn-Si system is constructed by evaluating the equilibrium phase diagrams of two related ternary systems: the Al-Fe-Si system (Figure 1a) and the Al-Mn-Si system (Figure 1b) [33]. The liquidus projection of the Al-Fe-Si system (Figure 1a) identifies stable compounds, including γ-τ_2, δ-τ_4, α-τ_5, and β-τ_6 [34]. Similarly, the Al-Mn-Si ternary system (Figure 1b) highlights the role of manganese (Mn) in suppressing the β-τ_6 phase, particularly in the presence of iron, thereby improving the mechanical properties of cast components [28].
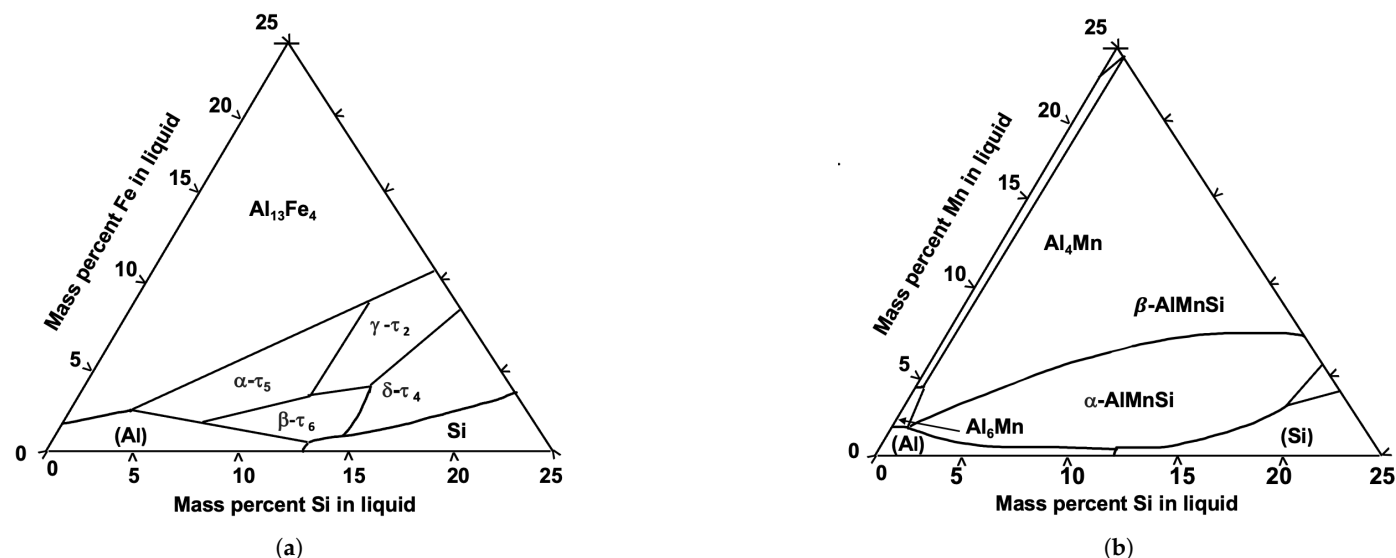
Figure 1. (**a**) Liquidus projection of the Al-Fe-Si ternary system and (**b**) Al-Mn-Si ternary system [28].

In the Al-Fe-Mn-Si system, two significant phases, α-AlMnSi and β-AlMnSi, have been identified. Zakharov et al. [35] reported a stable FCC-structured phase, $(Al_{16}(Mn, Fe)_4Si_3)$, alongside previously identified compounds $(Al_8FeMnSi_2)$ [36] and $(Al_{11.8}FeMn_{1.6}Si_{1.6})$ [37]. Although α-AlMnSi was initially observed in the ternary Al-Mn-Si system, it extends into the quaternary system as β-AlMnSi (Please note that β-AlMnSi is named as beta-AlMnSi by Thermo-Calc). However, no distinct or stable quaternary phases have been independently confirmed [28,38].

The COST-507 database [33] includes models for α-AlMnSi and β-AlMnSi, incorporating Fe solubility changes within the Mn sub-lattice [28]. Proposed chemical compositions, such as $(Al_{16}(Fe, Mn)_4Si_1(Al, Si)_2)$ for α-AlMnSi and $(Al_{15}Si_1(Al, Si)_4(Fe, Mn)_6)$ for β-AlMnSi, provide improved phase descriptions but fail to fully capture order-disorder transitions or solubility variations [39].

Table 1 summarizes key equilibrium phases in the quaternary system, listing optimized parameters of the β-AlMnSi phase and corresponding experimental and calculated data [28].

Table 1. Optimized Parameters for the β-AlMnSi Phase in the Quaternary System.

Phases	Fixed Composition [in wt.-%]	Experimental Values	Calculated Values
$Al_{13}Fe_4$, β-AlMnSi	$w_{Mn} = 0.04$, $w_{Si} = 0.02$	737 °C, $w_{Fe} = 0.03$	747 °C, $w_{Fe} = 0.032$
Al_6Mn, β-AlMnSi, Si	$w_{Fe} = 0.02$, $w_{Si} = 0.01$	697 °C, $w_{Mn} = 0.03$	728 °C, $w_{Mn} = 0.039$
α-AlMnSi, β-AlMnSi	$w_{Fe} = 0.01$, $w_{Si} = 0.04$	687 °C, $w_{Mn} = 0.035$	716 °C, $w_{Mn} = 0.0035$

Thermodynamic validation indicates that β-AlMnSi serves as an extended quaternary phase derived from the ternary Al-Mn-Si system, maintaining equilibrium with two classical eutectic phases: FCC-A1 and $Al_{13}Fe_4$. This study simulates the four-phase reaction $L \rightarrow Al_{13}Fe_4 + FCC\text{-}A1 + beta\text{-}AlMnSi$ to further explore phase transformations.

3. Materials and Methods

Multi-Phase-Field Model Coupled to CALPHAD Database

The phase field approach [40] is a well-established numerical simulation technique used to model the microstructural evolution of materials during phase transformations. This method employs "diffuse interface models" to resolve interactions between phases. Each thermodynamic phase or grain is represented as a field variable, denoted by

$\phi_i(x, y, z, t)$, which undergoes a dynamic transition from 0 to 1 across a diffuse, continuous interface separating two phases. Importantly, the total magnitude of all phase-field variables within any phase region is constrained to 1 [21].

$$\sum_{\alpha=1}^{N} \phi_\alpha(x, y, x, t) = 1 , \tag{1}$$

The number of phases present in each discrete volume is denoted by N. The phase variable represents the temporal evolution of the microstructure. The criterion for minimizing the total free energy density of the system is defined as follows:

$$F = \int_{\Omega} f \, dV = \int_{\Omega} (f_{int} + f_{chem}) \, dV , \tag{2}$$

The description of all terms in the multi-phase-field model requires the integration of various physical phenomena, including interfacial energy (f_{int}) and chemical energy (f_{chem}), over the entire volume of the system. The free energy densities associated with interfacial and chemical contributions are expressed as follows:

$$f_{int} = \sum_{\alpha=1}^{N} \sum_{\beta>\alpha}^{N} \frac{8\sigma_{\alpha\beta}}{\eta} \left[\frac{-\eta^2}{\pi^2} \nabla\phi_\alpha . \nabla\phi_\beta + \phi_\alpha\phi_\beta \right] , \tag{3}$$

$$f_{ch} = \sum_{\alpha=1}^{N} \phi_\alpha f_\alpha(c_\alpha) + \mu \left[c - \sum_{\alpha=1}^{N} (\phi_\alpha c_\alpha) \right] , \tag{4}$$

The interfacial free energy terms, f_{int}, are formulated based on the numerical interface width, η, which is chosen according to the characteristic length scale of the problem, and the interfacial energy, between the α phase and β phase. The chemical free energy terms, f_{ch}, include contributions such as the bulk free energy, f_α, of the α phase and its dependence on the concentration, c_α, represented as $f_\alpha(c_\alpha)$. Furthermore, the chemical potential (μ) or potential diffusivity is introduced as a Lagrange multiplier to ensure that the mass balance between the phases remains unchanged.

Finally, the equation governing the evolution of the phase is derived based on the principle of free energy minimization,

$$\dot{\phi} = -\frac{1}{N} \sum_{\alpha=1\neq\beta}^{N} M_{\alpha\beta} \left[\frac{\delta F}{\delta\phi_\alpha} - \frac{\delta F}{\delta\phi_\beta} \right] . \tag{5}$$

Within in the MPF framework, this equation is expanded into,

$$\dot{\phi}_\alpha = - \sum_{\beta=1...,N} \frac{M_{\alpha\beta}}{N} \left[\sum_{\gamma=1,...,N} (\sigma_{\alpha\gamma}^* - \sigma_{\beta\gamma}^*) I_\gamma + \frac{\pi^2}{8\eta} \Delta g_{\alpha\beta} \right] . \tag{6}$$

where,

$$I_\gamma = \nabla^2\phi_\gamma + \frac{\pi^2}{\eta^2}\phi_\gamma , \tag{7}$$

$$\Delta g_{\alpha\beta} = \Delta T_{\alpha\beta} \Delta s_{\alpha\beta} , \tag{8}$$

$$\Delta T_{\alpha\beta} = m_{\alpha\beta}(c_\alpha - c_\alpha^{eq}) , \tag{9}$$

The definitions of the parameters used in these equations are as follows: The number of phase fields is denoted by N; for example, (N = 2) for dual interfaces and (N = 3) for triple junctions. The term I_γ represents the generalized curvature. The mobility of the interface

between the α and β phases is denoted by $M_{\alpha\beta}$. The length scale of the numerical interface width, η, is related to the simulation resolution. The interface stiffness between the α and β phases is described by σ^*, while the driving force between the phase pair $\alpha\beta$ is represented by $\Delta g_{\alpha\beta}$. The parameter for local undercooling due to solute distribution is denoted by $\Delta T_{\alpha\beta}$. The equilibrium slope, $m_{\alpha\beta}$, is calculated by linearizing the phase diagram surface at the equilibrium state. The local composition in phase α is represented by c_α, and the equilibrium composition is denoted by c_i. The interface driving force, $\Delta g_{\alpha\beta}$, is derived from a quasi-equilibrium condition, where the local undercooling $\Delta T_{\alpha\beta}$ corresponds to the deviation in solute composition from the equilibrium composition. $\Delta S_{\alpha\beta}$ is defined as the difference in entropy between the α and β phases.

In multicomponent systems, an essential requirement is the formulation of diffusion equations for each solute element. The complexity arises due to the interdependence of these diffusion equations, which are interconnected through cross terms. In this framework, the total composition, c_i is treated such that the interface contains the phase compositions, c_i^α, of all constituting phases α. This capability facilitates simulations at the micrometer scale. Furthermore, thermodynamic information is obtained from the COST-507 database using the CALPHAD method, implemented in Thermo-Calc software version 2021b. This approach enables the calculation of phase diagrams by deriving the formula for single-phase Gibbs energy, considering pressure, temperature, and composition as variables in the equations [41]. The phase field model extends the CALPHAD approach and is employed to investigate the thermodynamic and kinetic properties of materials [42–44]. This method allows for the examination of capillarity effects, phase and grain boundaries, and diffusion phenomena, particularly under non-equilibrium conditions [41].

The multi-phase-field (MPF) model incorporates a diffusion equation to represent the evolution of solute composition across phases.

$$\dot{c}^i = \nabla \left(\sum_{\alpha=1}^{N} \phi_\alpha [D_\alpha^{ij} \nabla c_\alpha^j] + \left(\sum_{\alpha,\beta=1} j_{\alpha\beta}^i \right) \right), \tag{10}$$

The summation constraint is defined as:

$$\sum_\alpha \phi_\alpha c_\alpha^i = c^i \tag{11}$$

While, the phase compositions are obtained by imposing the condition of equilibrium partition coefficient,

$$c_\beta^i = k_{\alpha\beta}^i c_\alpha^i \tag{12}$$

In Equations (10)–(12), c^i represents the total composition of solute element i, whereas c_α^i and c_β^i represent the phase compositions of the solute element i in phase α and β, respectively. The equilibrium partition coefficient is given by $k_{\alpha\beta}^i$ and the diffusion coefficient D_α^{ij} is derived from the kinetic database. The term $j_{\alpha\beta}^i$ represents the anti-trapping current, which is designed to minimize systematic errors caused by the diffuse interface and variations in solute diffusivity between the solid and liquid phases, denoted as $\alpha\beta$. The full description of anti-trapping term for multicomponent alloy system can be found in [21,41].

Thermodynamic minimization is essential for determining phase concentrations based on the mixture concentration and individual phase fractions derived from the phase fields. However, performing quasi-equilibrium computations at every time step can impose significant computational demands. To enhance efficiency, intermittent quasi-equilibrium calculations are carried out, depending on the characteristics of the phase transformation. Between these calculations, the established quasi-equilibrium serves as the basis for constructing a local linear approximation of the equilibrium boundaries between phases. This

approach allows for the determination of key thermodynamic parameters, including the driving force, phase balance, substance distribution among phases, and the composition of each phase [45,46].

The system temperature is updated using the frozen temperature method, which accounts for a constant thermal gradient and cooling rate [47]. The complete set of equations describing the interconnected phase field model, as discussed above, has been implemented in the "OpenPhase" software package [48].

4. Simulation Set Up and Material Input Data

The model employed in this study is the multicomponent multi-phase-field (MPF) model developed by Steinbach and co-workers [21,46], implemented using the OpenPhase software version 4.7. For the simulation, a 3D box with dimensions of $60 \times 60 \times 120$ grid cells and a grid resolution of 1×10^{-7} m was considered. At the start, the simulation box is assumed to be entirely filled with liquid phase at a temperature above the liquidus. Due to the limited size of the simulation domain, the calculations are restricted to the scale of multiple dendrite growth within a single grain. As the solidification progresses, multiple seeds of primary phase (FCC-A1) and precipitates ($Al_{13}Fe_4$ and beta-AlMnSi) are allowed to nucleate in the simulation domain. While precipitates are permitted to nucleate throughout the domain, the primary phase is restricted to grow only from the bottom surface, replicating the epitaxial growth typically observed in directional solidification. It is worth noting that each surviving seed is assigned a unique order parameter, although the phase fields of the same phase are allowed to merge or collapse due to competitive growth. Table 2 presents the optimized physical and numerical parameters used in the simulation. It also provides details on the global cooling rate, thermal gradient along the Z-axis, and initial temperature. For the simulation, a 3D box with size of $60 \times 60 \times 120$ grid cells and a grid resolution equal to 1×10^{-7} m was considered.

Nucleation was modeled based on AL Greer's approach [49,50], which relates the formation of nuclei to the local driving force exceeding the nucleation barrier. Depending on the nucleation density set for the nucleating phase, the model initially plants the nucleation seeds of the phase in the matrix phase. However, the seeds are allowed to grow only when the local driving force (ΔG_{local}) calculated from Equation (8) exceeds the curvature undercooling. This relationship is expressed by the following formula:

$$\Delta G_{local} \geq \frac{2\sigma_{max}}{r} \, , \tag{13}$$

where, σ_{max} is the interface energy and r is the radius of the seed.

Table 2. Optimized numerical and physical parameters employed for 3D phase field simulations.

Parameter Description	Symbol	Value
Box size (x-direction)	L_x	60
Box size (y-direction)	L_y	60
Box size (z-direction)	L_z	120
Grid spacing	Δx	1×10^{-7} m
Numerical time increment	Δt	1×10^{-6} s
Diffuse interface width	η	4.5×10^{-7} m
Initial temperature	T_0	927 K
Cooling rate	$\frac{dT}{dt}$	-100 K/s
Thermal gradient along z-axis	G_z	10,000 K/m
Interface mobility: Liquid to FCC-A1	M_{01}	0.750×10^{-9} m^4/J·s
Interface mobility: Liquid to $Al_{13}Fe_4$	M_{02}	1.03×10^{-11} m^4/J·s
Interface mobility: Liquid to beta-AlMnSi	M_{03}	1×10^{-10} m^4/J·s
Interface mobility: FCC-A1 to $Al_{13}Fe_4$	M_{12}	1.03×10^{-10} m^4/J·s
Interface mobility: FCC-A1 to beta-AlMnSi	M_{13}	1.03×10^{-10} m^4/J·s
Interface mobility: $Al_{13}Fe_4$ to beta-AlMnSi	M_{23}	3.03×10^{-14} m^4/J·s

4.1. Effective Mobility

Determining accurate values for interface mobility is essential for the material input data. In this study, the effective interface mobility between different phase pairs is calculated using the equation provided in [21], defined as:

$$\mu^{eff} = \mu \left/ \left(1 + \mu \frac{\eta}{8} \Delta S m_l [D_l^{ij}]^{-1} (c_s^j - c_l^j) \right) \right. ,$$

(14)

The effective mobility, μ^{eff}, between two phases is calculated based on the chemical diffusion coefficients (D_l^{ij}), the entropy difference (ΔS) between the phases, the composition of each element at two different temperatures within each phase ($c_s^j - c_l^j$), and the slope (m_l) between two equilibrium phases in the liquid. These values are derived from the results of phase-field simulations.

4.2. Material Input Data

The nominal composition of the quaternary Al-Fe-Mn-Si system, as presented in Table 3, is derived from the experimental reference [51]. Figure 2 indicates phase formation in the Al-Fe-Mn-Si system under equilibrium (lever rule) and non-equilibrium (Scheil–Gulliver) conditions was calculated using Thermo-Calc version 2021b, employing the thermodynamic database (tdb-file) provided by Hallstedt and co-workers [52].

Table 3. Chemical composition of multi component alloys Al-Fe-Mn-Si utilized in phase-field simulation.

Elements	Al	Mn	Fe	Si
Composition (Weight %)	Bal	2.7	1.223	0.04
Composition (Mol %)	Bal	1.353	0.603	0.039

(a)

(b)
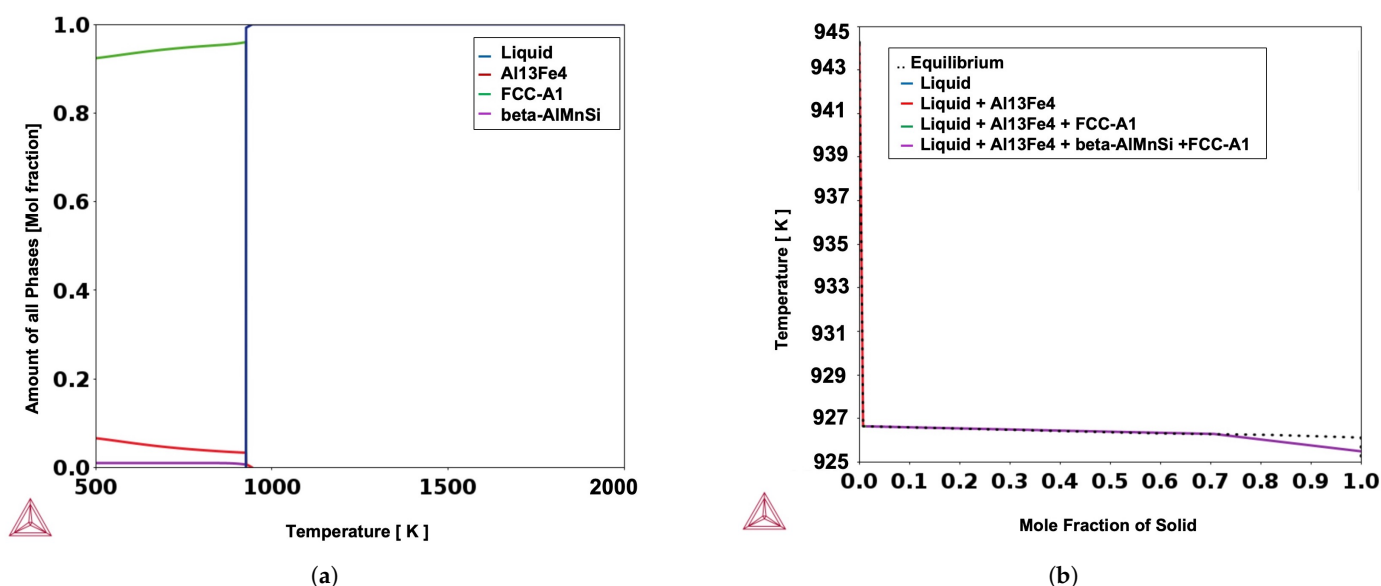
Figure 2. Calculation of stable phase fractions: (**a**) under equilibrium conditions as a function of temperature based on the element percentages in Table 3, and (**b**) using Scheil-Gulliver solidification based on the element contents in Table 3.

4.2.1. Formation of Intermetallic Phases at Equilibrium Condition in Multicomponent Al-Fe-Mn-Si System

This multicomponent system comprises Al, Si, Fe, and Mn. The formation of phase compounds is influenced by the temperature and concentration of these elements. In this

system, stable equilibrium phases at specific compositions and temperature conditions can be identified using the phase diagram.

Figure 3 presents three isopleth phase diagrams illustrating the variation in the percentages of Fe, Mn, and Si with respect to temperature. In Figure 3a, the cross point on the diagram at approximately 1.223 wt.% Fe indicates the formation of phases during solidification, which includes: (i) the appearance of the intermetallic $Al_{13}Fe_4$ phase at high temperature as the first solid phase, (ii) the nucleation of FCC-A1, and (iii) the formation of beta-AlMnSi. Figure 3b,c depict the stability of equilibrium phases with respect to temperature for varying Mn and Si contents on the isopleth phase diagrams.

In this work, the Mn content was set at 2.7 wt.%, while the Si content was maintained at less than 1 wt.%. It is worth noting that, in this multicomponent alloy, the chemical composition adjustments of the elements play a critical role in determining the eutectic transformation. The eutectic transition in multicomponent alloys is characterized by the production of the initial solid phase during solidification, which dictates whether the phase transformation is hypo or hyper eutectic. The nucleation of $Al_{13}Fe_4$ as the initial intermetallic phase in this system confirms the hyper-eutectic transition. Additionally, the formation of beta-AlMnSi as a quaternary phase verifies the presence of two distinct reactions in this system.

(**a**) Fe isopleth

(**b**) Mn isopleth
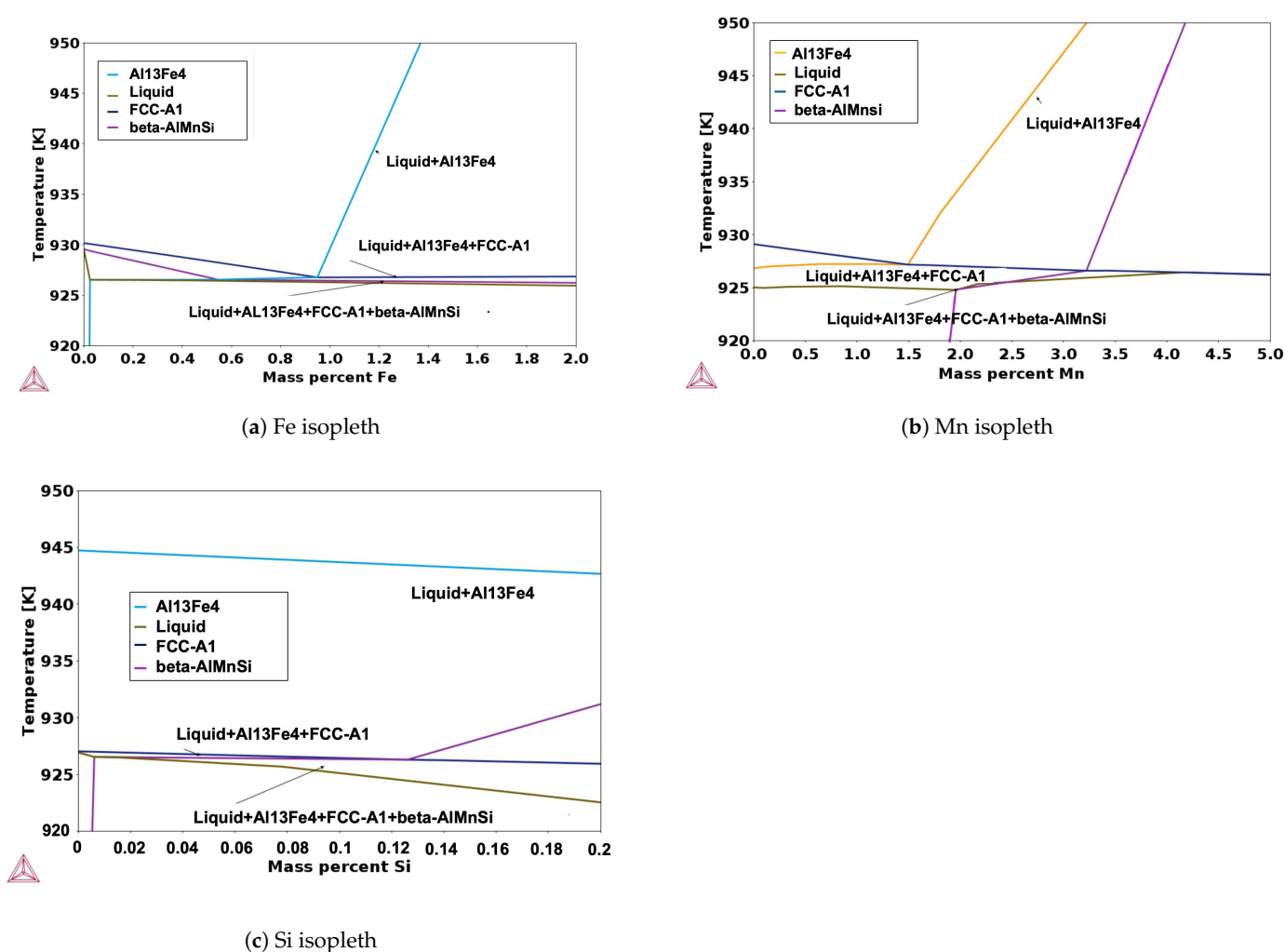
(**c**) Si isopleth

Figure 3. The isopleth phase diagrams (**a**–**c**) show the nucleation and growth of FCC-A1, $Al_{13}Fe_4$, and β-AlMnSi from the undercooled liquid. The X-axis represents the chemical composition of (**a**) Fe, (**b**) Mn, and (**c**) Si with respect to temperature.

4.2.2. Initial Si Composition Adjustment

After performing phase diagram calculations for the quaternary system using Thermo-Calc, the model was transformed into a triangular representation. In this model, Si and Mn were positioned along the sides in regions with high Al concentrations, as shown in Figure 4. The equilibrium stability of the liquid, FCC-A1, $Al_{13}Fe_4$, and beta-AlMnSi phases in this system is observed when the Si concentration is 0.04 wt.% and the Mn content is 2.5 wt.%. Consequently, these values were chosen for this study.

Phase diagram calculations for the quaternary system were performed using Thermo-Calc, and the model was subsequently transformed into a triangular representation. In this model, Si and Mn were positioned along the sides in regions with high Al concentrations, as illustrated in Figure 4. The equilibrium stability of the liquid, FCC-A1, $Al_{13}Fe_4$, and beta-AlMnSi phases in this system is evident when the Si concentration is 0.04 wt.% and the Mn content is 2.5 wt.%. These values were, therefore, chosen for this study.
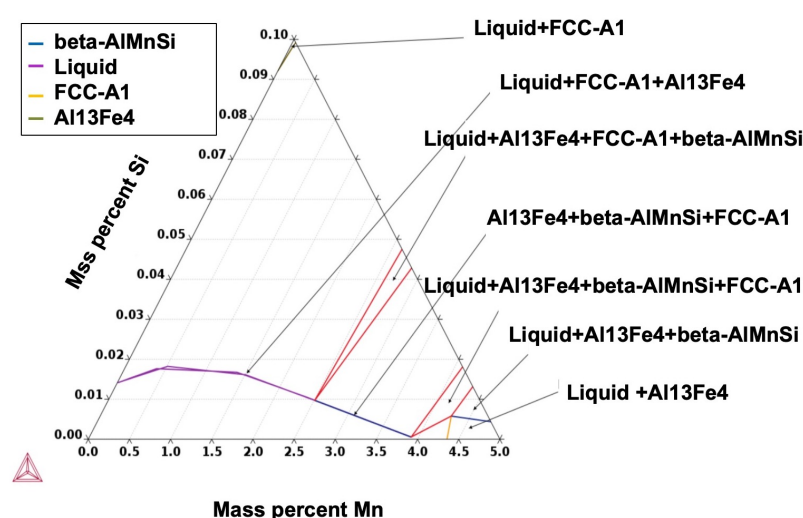
Figure 4. FCC-A1, $Al_{13}Fe_4$ and beta-AlMnSi with liquid in alloy Al-Fe-Mn-Si system while Mn and Si elements are on the triangle sides in the rich corner aluminum.

5. Results

This section presents detailed insights from phase-field simulations on the evolution of the primary phase and the simultaneous formation of multiple precipitates as eutectic phases [53]. In the current 3D phase field simulation, eutectic solidification is investigated through two distinct reactions. The first reaction, $L \rightarrow (Al_{13}Fe_4) + (FCC-A1)$ results in the nucleation and growth of the $Al_{13}Fe_4$ precipitate phase and the rod-shaped FCC-A1 phase. The second reaction involves the nucleation of the quaternary phase (beta-AlMnSi) from the residual liquid within the simulation box. These simulations demonstrate the capability of the 3D multi-phase-field approach to analyze the nucleation and spatial distribution of equilibrium solid phases and microstructures in the quaternary Al-Fe-Mn-Si system. The initial condition of the simulation assumes the system is completely filled with liquid phase, with the nominal composition provided in Table 3. The system's initial temperature is set to 927 K, where only the liquid phase is stable. Solidification in the multicomponent system begins with the emergence of the intermetallic phase $Al_{13}Fe_4$ within the undercooled liquid melt.

Figure 5 illustrates the nucleation and growth of the $Al_{13}Fe_4$ phase at three different time steps: (a) $t_0 = 0.0195$ s, (b) $t_1 = 0.031$ s, and (c) $t_2 = 0.052$ s. The $Al_{13}Fe_4$ phase is recognized as a high-temperature precipitate in aluminum systems [54]. In this multi-phase-field simulation, the amount of this precipitate is less than 4%. The nucleation and

growth of the $Al_{13}Fe_4$ phase are observed throughout the simulation box, appearing in a spherical shape.

These observations suggest that the diffusivity of Fe and Mn atoms plays a critical role in the formation of this intermetallic phase at high temperatures, whereas Si atoms cannot diffuse into this phase. However, it is inevitable to account for the presence of Si as an impurity in the $Al_{13}Fe_4$ phase [55]. Furthermore, during the formation of the intermetallic $Al_{13}Fe_4$ phase in the liquid, supersaturation of Fe and Mn elements occurs. Notably, this phase strongly rejects Si, indicating that Si is not thermodynamically favorable in its structure.
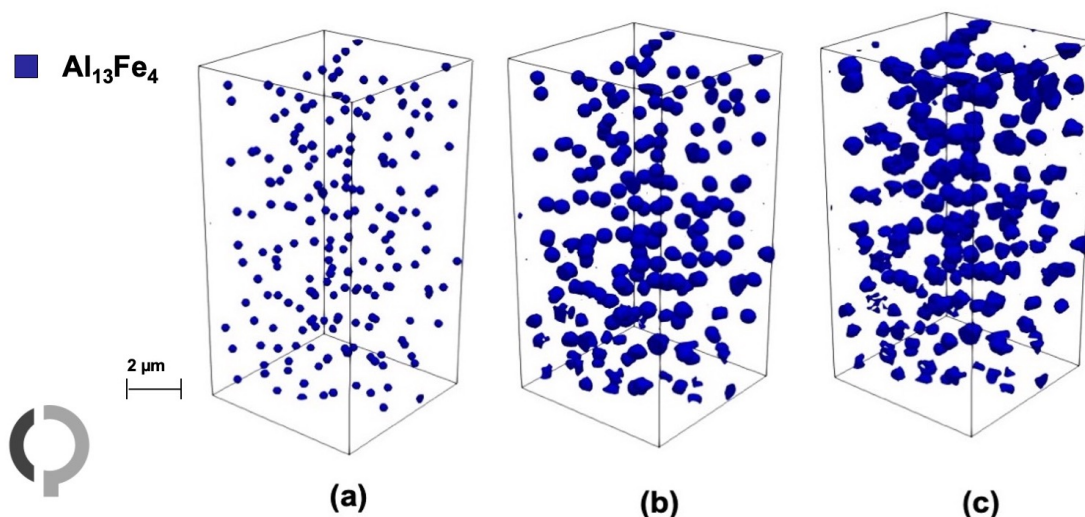
Figure 5. (**a**) Nucleation of $Al_{13}Fe_4$ at $t_0 = 0.0195$ s, (**b**) growth of this precipitate at $t_1 = 0.031$ s, (**c**) completion of the precipitate at $t_2 = 0.052$ s.

As shown in Table 2, the nucleation of the FCC-A1 phase is permitted at the bottom of the simulation box along the Z direction. The largest domain within the simulation box is occupied by the FCC-A1 eutectic phase, which forms in a rod-like or lamellar structure. Figure 6 illustrates the evolution of the FCC-A1 eutectic phase at three distinct time steps: (a) nucleation of FCC-A1 at $t_0 = 0.0255$ s, (b) growth at $t_1 = 0.031$ s, and (c) the phase nearing the completion of solidification at $t_2 = 0.052$ s. This phase is recognized as the primary phase in the casting of aluminum systems.

The simulation reveals restricted diffusion of silicon atoms within the liquid during the formation of the FCC-A1 phase. Experimental studies indicate that the growth of lamellae transitions from an unstable state to a metastable state and eventually stabilizes as the spacing between lamellae increases [53]. However, the simulation results show that the growth of the lamellar remains unstable. This instability can be attributed to the limitations in the size of the simulation box.

Furthermore, during the formation of the FCC-A1 phase, silicon saturation occurs in the liquid, while this primary phase rejects Fe and Mn atoms. These observations highlight the phase's unique interaction with the surrounding liquid environment and its role in solidification dynamics.

The formation of the third quaternary phase, beta-AlMnSi, is a result of the second eutectic reaction. Thermodynamic calculations indicate that, in the selected alloy system, the amount of this quaternary phase is less than 1%. This phase exhibits distinct characteristics compared to the intermetallic and primary phases. Notably, there is a significant diffusion of Mn atoms and a marked depletion of Fe in this phase. Additionally, Si atoms can dissolve in this quaternary phase, albeit to a limited extent. Figure 7 illustrates the

nucleation of beta-AlMnSi within the undercooled liquid at the interface between FCC-A1 and $Al_{13}Fe_4$ at three different time steps: (a) $t_0 = 0.039$ s, (b) $t_1 = 0.04$ s, and (c) $t_2 = 0.052$ s. This quaternary phase can be distinguished from the intermetallic and primary phases based on two key features. First, the supersaturation of Mn and Si elements occurs at the interface between FCC-A1 and $Al_{13}Fe_4$ during the nucleation and growth of beta-AlMnSi. Second, the Fe element is actively rejected by this phase during its formation. These behaviors highlight the unique thermodynamic and kinetic properties of beta-AlMnSi in the Al-Fe-Mn-Si system.
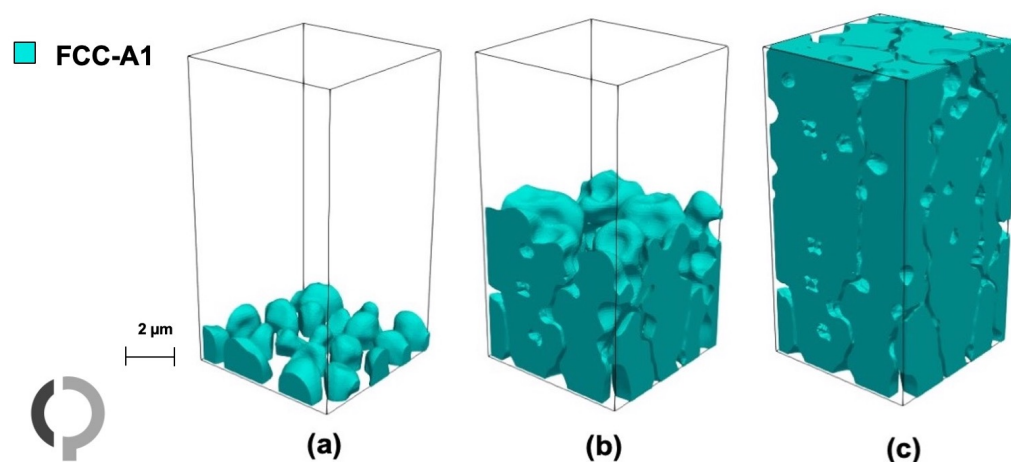

Figure 6. (**a**) Nucleation of FCC-A1 at $t_0 = 0.0255$ s, (**b**) growth of this phase at $t_1 = 0.031$ s, and (**c**) completion of the solid phase at $t_2 = 0.052$ s.
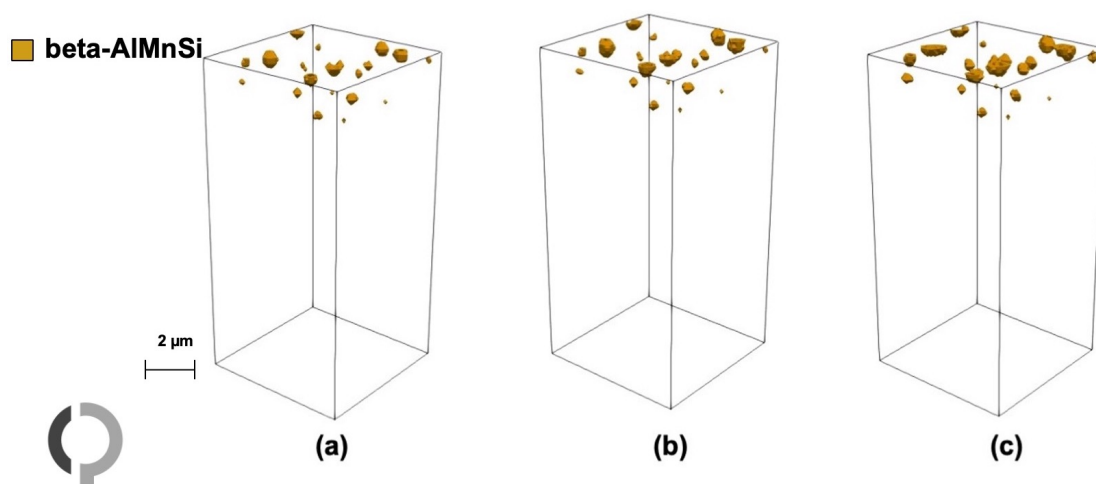
Figure 7. (**a**) Nucleation of beta-AlMnSi at $t_0 = 0.039$ s, (**b**)$t_1 = 0.04$ s growth of this phase at, and (**c**) completion of the phase at $t_2 = 0.052$ s.

Figure 8 illustrates the sequential nucleation and growth of the $Al_{13}Fe_4$, FCC-A1, and beta-AlMnSi phases, emphasizing their spatial distribution and interactions as observed in the simulation.
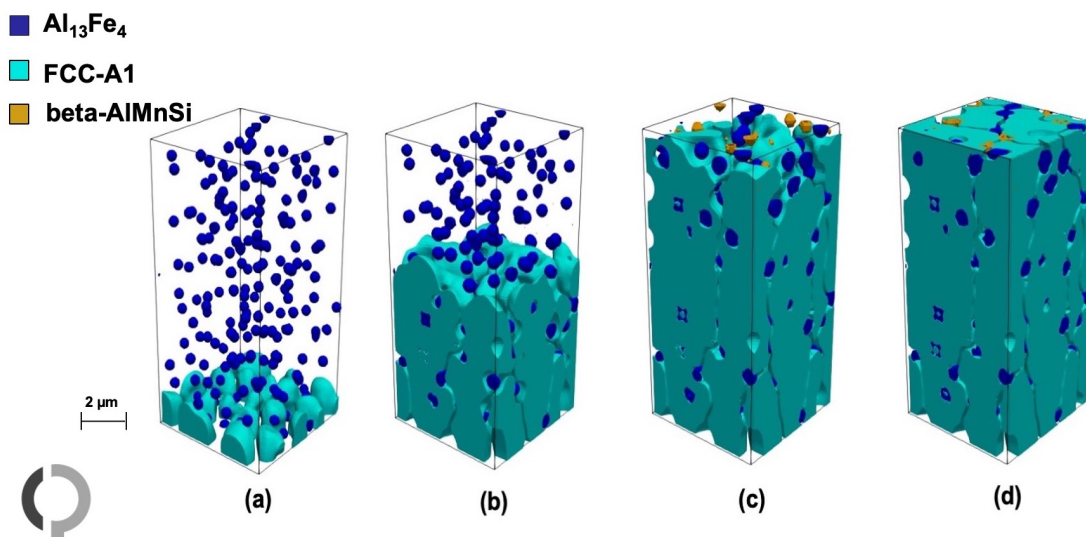
Figure 8. Microstructure evolution of the multicomponent Al-Fe-Mn-Si system during directional solidification via eutectic reactions at four different time steps: (**a**) $t_0 = 0.0255$ s, (**b**) $t_1 = 0.032$ s, (**c**) $t_2 = 0.039$ s and (**d**) $t_3 = 0.052$ s, showing the phase fractions of $Al_{13}Fe_4$ (dark blue), FCC-A1 (light blue), and beta-AlMnSi (orange) in the multi-phase-field simulation.
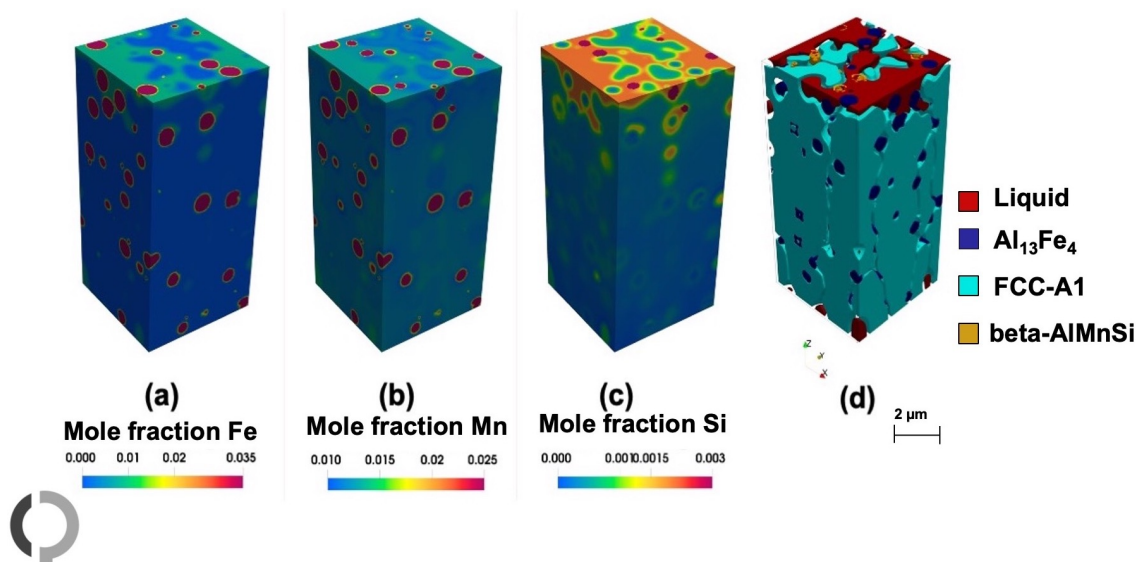
5.1. Elemental Distribution of Alloying Elements

Macro-segregation and micro-segregation are critical factors to consider during the directional solidification of multicomponent aluminum alloys. The distribution of each element significantly influences material properties, impacting the homogeneity and composition of secondary phase precipitates. Both macro-segregation and micro-segregation patterns can be observed in alloying elements during the solidification process.

The multi-phase-field (MPF) model offers a substantial advantage in its ability to accurately replicate the spatial arrangement of components in 3D [41,56]. Understanding segregation is particularly crucial in the multicomponent Al-Fe-Mn-Si system, where it plays a key role in determining microstructural and compositional outcomes.

This section analyzes the simulation results to determine the elemental distribution of alloying elements across various phases. Figure 9 illustrates the solute segregation of alloying elements at the end of solidification ($t = 0.04$ s), along with the corresponding morphology.

As shown in Figure 9, alloying elements such as Fe and Mn, which act as stabilizers for the $Al_{13}Fe_4$ intermetallic phase, exhibit higher enrichment in this phase compared to the primary FCC-A1 phase. The segregation of Mn in the beta-AlMnSi quaternary phase results in an enriched concentration profile. Consequently, Fe atoms are concentrated in $Al_{13}Fe_4$ while being depleted in the FCC-A1 and beta-AlMnSi phases. Silicon shows slight segregation in the FCC-A1 and $Al_{13}Fe_4$ phases but is notably depleted in the $Al_{13}Fe_4$ intermetallic precipitate [56].

Figure 9. Concentration distribution of all solute components in the multicomponent Al-Fe-Mn-Si system (**a**) Fe, (**b**) Mn, (**c**) Si at $t = 0.04$ s. (**d**) the morphology with phase information is shown on the right.

5.2. Distribution of Alloying Elements in Each Phase Pair

5.2.1. $Al_{13}Fe_4$ and Liquid

Figure 10 presents a section of the simulation box, illustrating the total mole fraction of (a) Fe, (b) Mn, and (c) Si, corresponding to the volume fractions of the liquid phase and the $Al_{13}Fe_4$ intermetallic phase, as shown in Figure 10. Additionally, Figure 11d,f depict the spatial distribution of Fe, Mn, and Si concentrations within the liquid phase and the intermetallic compound $Al_{13}Fe_4$.
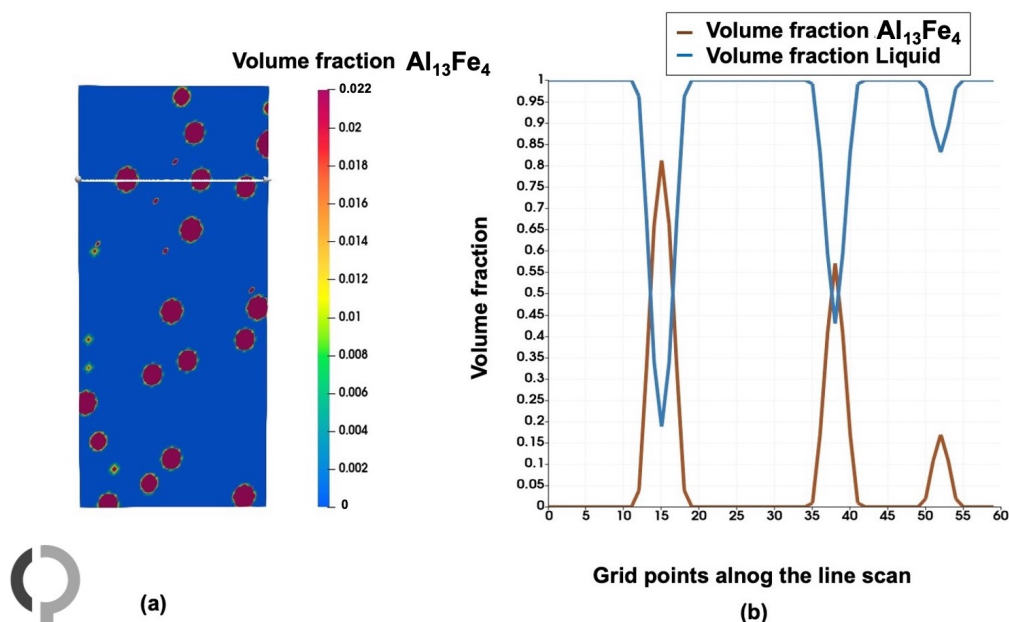
**Figure 10.** (**a**) Line scan of the volume fraction of $Al_{13}Fe_4$ along the white line. (**b**) Depicts the volume fractions of $Al_{13}Fe_4$ and the liquid phase.

The phase denoted as $Al_{13}Fe_4$ originates from the binary Al-Fe system and persists in the ternary Al-Fe-Mn system. In this compound, some Mn atoms can substitute for Fe atoms, although Mn solubility is limited. Si atoms in the $Al_{13}Fe_4$ precipitate cannot exceed 2.5 wt % solubility [54]. A line scan of the simulation results reveals Mn segregation within

the $Al_{13}Fe_4$ precipitate, confirming experimental observations [54]. Additionally, while Fe segregation is observed, it is not complete, aligning with experimental findings that describe the phase composition as $Al_{13}Fe_4$ [54]. The Si element is notably depleted in this precipitate, further corroborating experimental data.
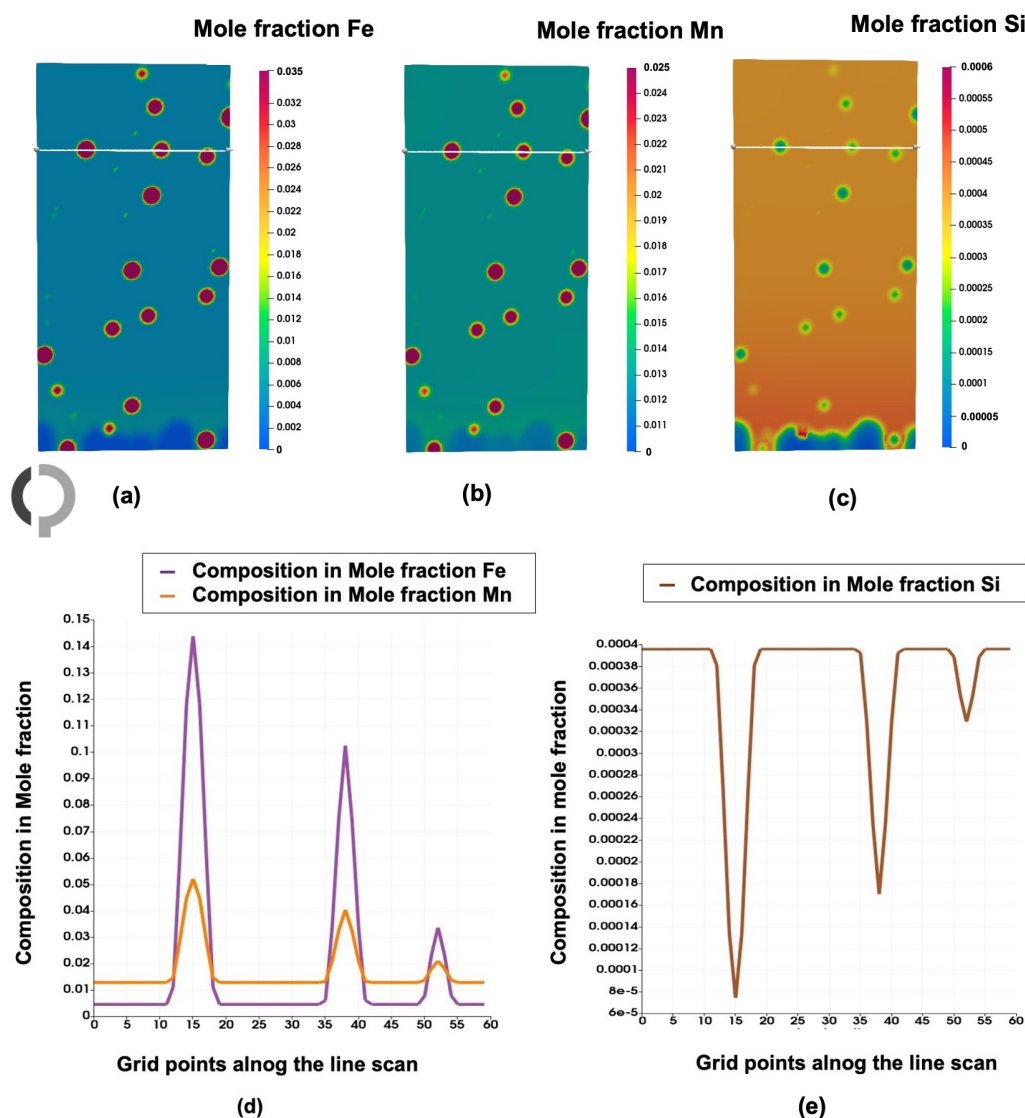
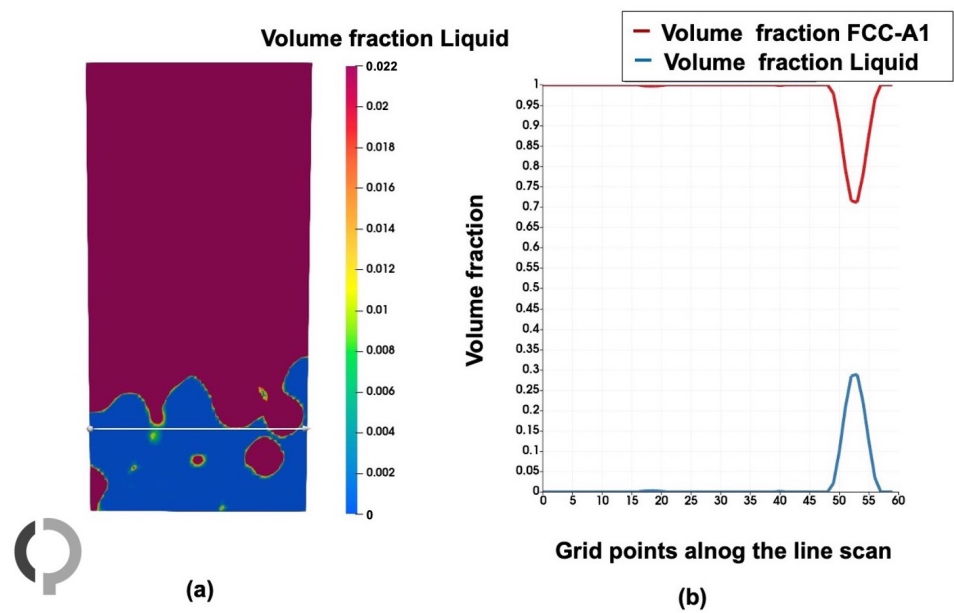**Figure 11.** Line scan of solute elements in the Al-Fe-Mn-Si system at a specific time step along the $Al_{13}Fe_4$ and liquid phases (shown by the white line). (**a**–**c**) Show the mole fractions of Fe, Mn, and Si, respectively. (**d**,**e**) highlights the phases presence, where Fe and Mn segregated, while Si is depleted.
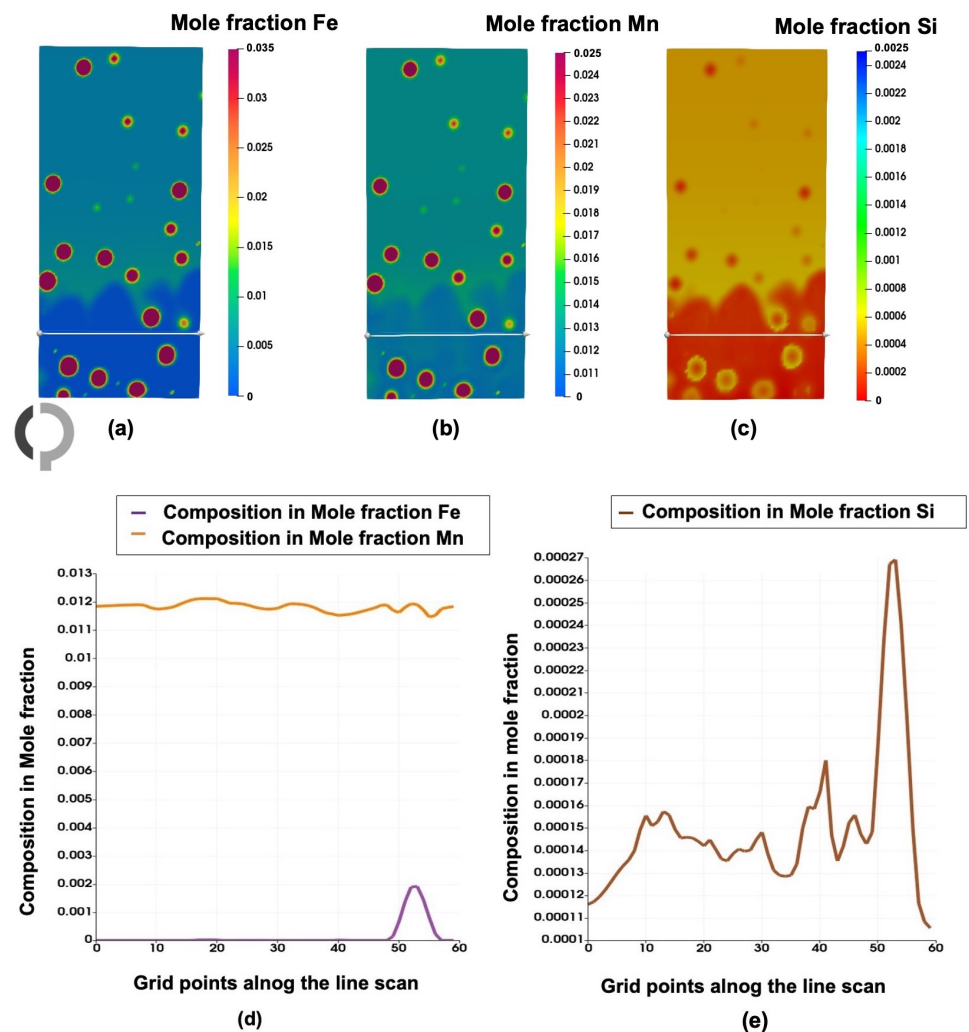
5.2.2. FCC-A1 and Liquid

Following the procedure described in Section 5.2.1, a line scan is generated, as shown in Figure 12, to illustrate the concentration profiles of (a) Fe, (b) Mn, and (**c**) Si corresponding to the volume fraction of the liquid phase and FCC-A1, as depicted in Figure 13.

The line scan in Figure 13d reveals that there is no diffusivity of iron (Fe) or manganese (Mn) atoms into the primary FCC-A1 phase, indicating depletion of Fe and Mn in this phase. Conversely, Figure 13e demonstrates the solubility of silicon (Si), which increases to a limited extent in the FCC-A1 phase.

Figure 12. (**a**) Line scan of the volume fraction of liquid along the white line. (**b**) Shows the volume fractions of FCC-A1 and the liquid phase.
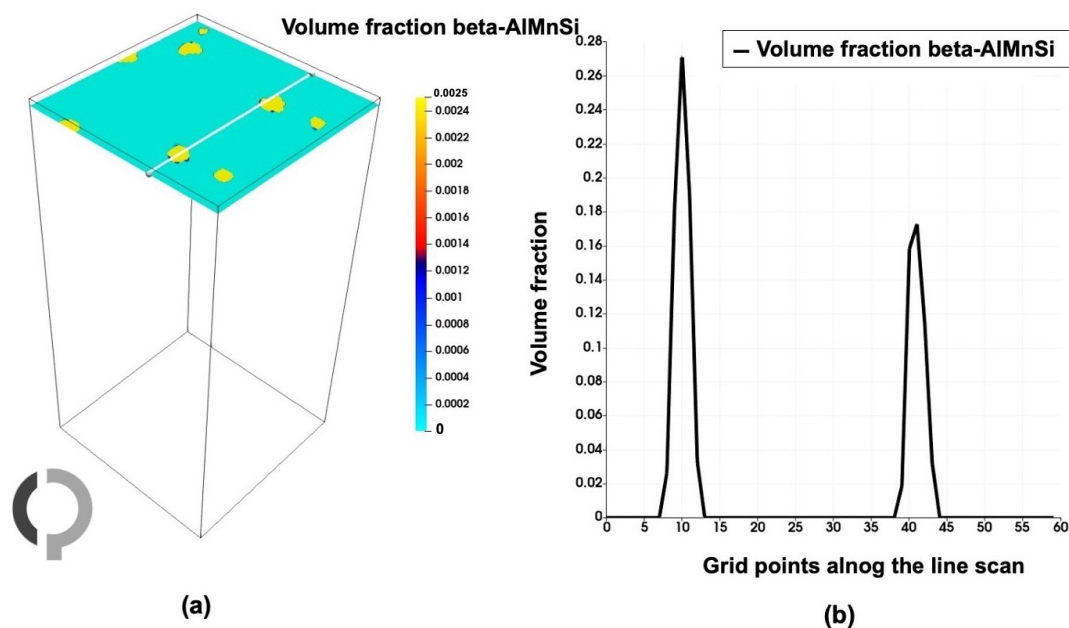

Figure 13. Line scan of solute elements in the Al-Fe-Mn-Si system at a specific time step along the FCC-A1 and liquid phases (shown by the white line). (**a**–**c**) Show the mole fractions of Fe, Mn, and Si, respectively. (**d**,**e**) highlights the phases presence, where Fe and Mn depleted, while Si is segregated.

5.2.3. Beta-AlMnSi and Liquid

As previously noted, the alloy system is quaternary. According to the Gibbs phase rule, three solid phases should form at the end of the eutectic reactions. Based on thermodynamic modeling, the quaternary Al-Mn-Fe-Si system does not exhibit a distinct new phase. Instead, it comprises a mixture of two ternary systems: Al-Mn-Si and Al-Fe-Si, which can result in the extension of the beta-AlMnSi phase [28]. At the conclusion of this simulation, the liquid phase, along with FCC-A1 and $Al_{13}Fe_4$, transforms into beta-AlMnSi through the second eutectic reaction.

In Figure 14, a line scan (white arrow) is used to analyze the presence of the quaternary beta-AlMnSi phase, following the same procedure as in the previous section.

The elemental distribution in the quaternary beta-AlMnSi phase during its formation and growth under directional solidification is analyzed in Figures 14 and 15. These line scans reveal that no Fe atoms are present in beta-AlMnSi, as all Fe atoms are replaced by Mn, leading to a significant depletion of Fe in this phase. Furthermore, Fe atoms were not observed in FCC-A1. Conversely, the total mole fraction of Mn increased in beta-AlMnSi and $Al_{13}Fe_4$, although not to the same extent as in the quaternary phase. Figure 15 shows the line scan of the beta-AlMnSi phase, where Fe exhibits low solubility, with mole fractions dropping to less than 0.01%. Mn shows significant segregation during the formation of the beta-AlMnSi phase, reaching a maximum of 0.22 mole % (equivalent to 36.48 wt.%). The mole fraction of Si also increases, indicating preferential incorporation or enrichment of Si in this phase. The depletion of Fe in the beta-AlMnSi phase suggests that most Fe atoms are replaced by Mn, resulting in the highest Fe depletion and Mn enrichment. This substitution and enrichment behavior distinguishes the beta-AlMnSi phase from being classified as an intermetallic phase. Furthermore, as highlighted in the literature section, the beta-AlMnSi phase is considered an extended phase, where Fe exhibits limited solubility while Mn effectively replaces Fe atoms. Several researchers have also reported varying observations on the solubility of Fe in this phase, further supporting the findings presented in this study.

(a)

(b)

Figure 14. (**a**) Line scan of the volume fraction of beta-AlMnSi (shown by white line). (**b**) Shows the volume fractions of beta-AlMnSi phase.
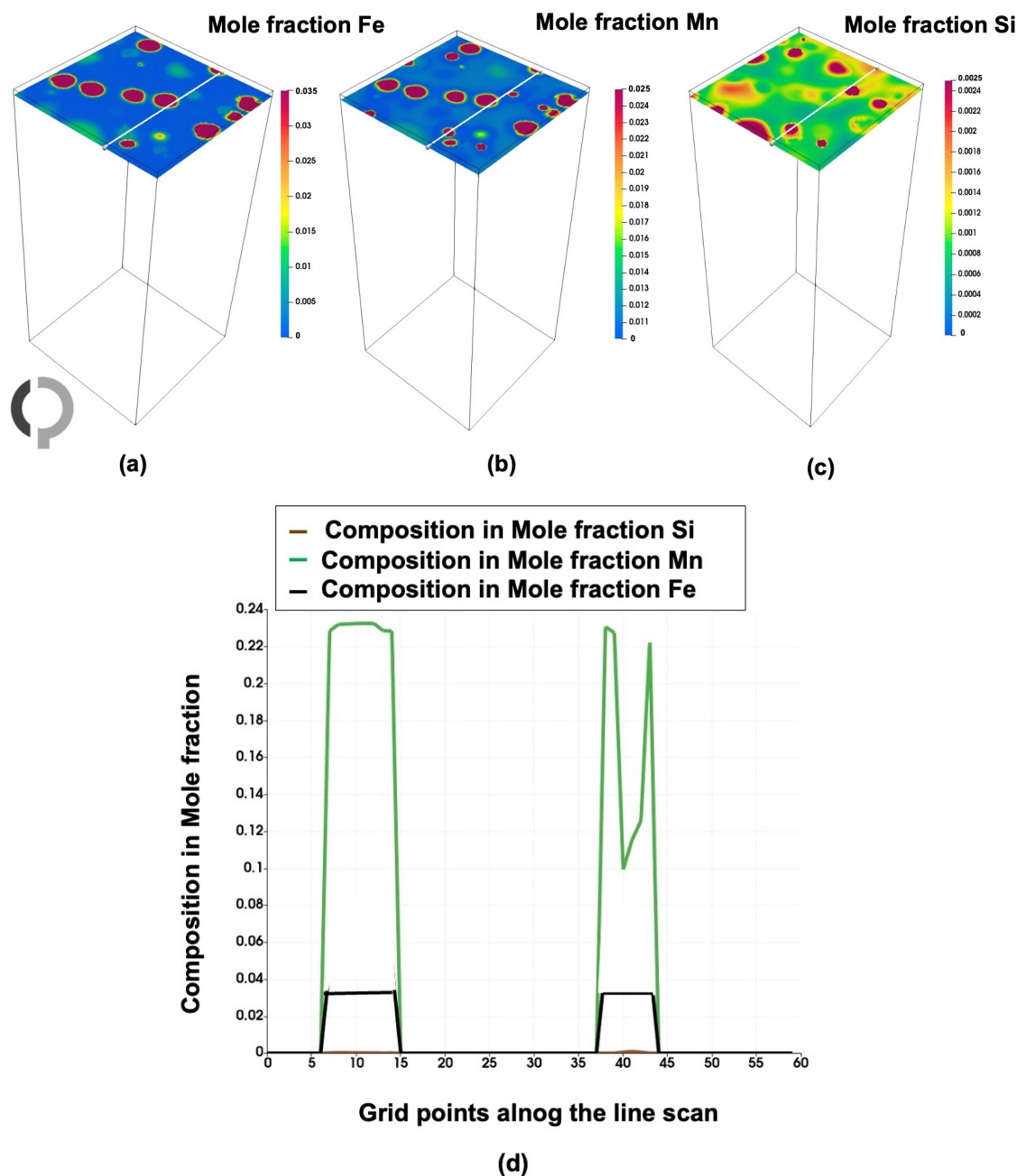
Figure 15. Line scan of solute elements in the Al-Fe-Mn-Si system at a specific time step along the beta-AlMnSi phase (indicated by the white line). (**a**–**c**) Show the mole fractions of Fe, Mn, and Si, respectively. (**d**) Highlights the phase presence, where Fe is depleted, while Si and Mn are segregated.

6. Summary & Conclusions

To summarize, the eutectic solidification morphology of the multicomponent Al-Fe-Mn-Si system under directional solidification conditions is investigated using a multi-phase-field model coupled with a CALPHAD thermodynamic database. The 3D microstructure selection map reveals the formation of three distinct solid phases. First, the intermetallic $Al_{13}Fe_4$ phase nucleates in the liquid. This is followed by the growth of the lamellar or rod-shaped primary eutectic FCC-A1 phase. Finally, when the liquid becomes supersaturated at the interface between FCC-A1 and $Al_{13}Fe_4$, the nucleation and growth of the quaternary beta-AlMnSi phase is observed. Additionally, by incorporating a kinetic database, the effects of multicomponent diffusion on eutectic solidification are thoroughly analyzed. Based on the results obtained from 3D phase-field simulations of the Al-Fe-Mn-Si

directional solidification process, along with the evolution of eutectic morphology and multicomponent segregation, the following conclusions are drawn.

- The simulation results indicate that, for the selected alloy system, solidification begins with the nucleation and growth of the spherical eutectic phase $Al_{13}Fe_4$ throughout the liquid. As solidification progresses and the system temperature decreases, the primary eutectic FCC-A1 phase forms along the growth direction. Subsequently, supersaturation of the remaining liquid leads to the nucleation of the quaternary beta-AlMnSi phase. The volume fractions of these phases, as obtained from the simulation results, closely align with the thermodynamic calculations performed using the open database for the Al-Fe-Mn-Si system.
- Elemental distribution analysis reveals significant variations in the segregation behavior of alloying elements in the Al-Fe-Mn-Si system. The elements Fe and Mn are primarily associated with the formation of the $Al_{13}Fe_4$ phase, while silicon (Si) is predominantly found in the primary eutectic FCC-A1 phase. The diffusivity of Mn and Si, acting as stabilizers in the quaternary beta-AlMnSi phase, exhibits an upward trend in concentration.
- The analysis of line scans at the eutectic phases reveals the distinct segregation behavior of Fe in the beta-AlMnSi phase. Initially, Fe exhibits a higher level of segregation into the liquid phase, which subsequently decreases as the liquid transforms into the quaternary beta-AlMnSi phase. A noticeable depletion of Fe is observed in this phase.
- Further research is required to quantify the influence of interface anisotropies across various phases. Additionally, the simulations in this study were designed with reference to both experimental data and thermodynamic modeling results. However, the obtained simulation results require direct validation through experimental studies conducted on the same alloy composition.

Author Contributions: Conceptualizations, K.N., I.S. and M.U.; methodology, K.N. and I.S.; Software, K.N., O.S. and D.I.; formal Analysis, K.N., M.U., I.S. and D.I.; Investigation, K.N. and I.S.; visualizations, K.N.; supervision, O.S. and I.S.; writing—original draft preparation, K.N.; writing—review and editing, D.I.;project administration, I.S.; funding acquisition, I.S. All authors have read and agreed to the published version of the manuscript.

Data Availability Statement: The data presented in this study are available on request from the corresponding author.

Conflicts of Interest: Authors Murali Uddagiri, Oleg Shchyglo, and Ingo Steinbach were employed by the company OpenPhase Solutions GmbH. The remaining authors declare that the research was conducted in the absence of any commercial or financial relationships that could be construed as a potential conflict of interest.

References

1. Chen, H.L.; Chen, Q.; Engström, A. Development and applications of the TCAL aluminum alloy database. *Calphad* **2018**, *62*, 154–171. [CrossRef]
2. Otani, L.B.; Soyama, J.; Zepon, G.; Costa e Silva, A.; Kiminami, C.S.; Botta, W.J.; Bolfarini, C. Predicting the formation of intermetallic phases in the Al-Si-Fe system with Mn additions. *J. Phase Equilibria Diffus.* **2017**, *38*, 298–304. [CrossRef]
3. Zolotorevsky, V.S.; Belov, N.A.; Glazoff, M.V. *Casting Aluminum Alloys*; Elsevier: Amsterdam, The Netherlands, 2007; Volume 12.
4. Callegari, B.; Lima, T.N.; Coelho, R.S. The influence of alloying elements on the microstructure and properties of Al-Si-based casting alloys: A review. *Metals* **2023**, *13*, 1174. [CrossRef]
5. Tian, N.; Wang, G.; Zhou, Y.; Liu, C.; Liu, K.; Zhao, G.; Zuo, L. Phase Formation and Microstructure Evolution of Al-5Si-0.8 Mg Alloys with Different Mn Concentrations. *Metals* **2021**, *11*, 308. [CrossRef]

6.   Zhenjie, C.; Haichang, J.; Duo, Z.; Qijuan, D.; Junjun, P.; Luanluan, J. Influence of Mn on the precipitates in 6082 aluminum alloy. *J. Mater. Sci.* **2024**, *59*, 9734–9748. [CrossRef]

7.   Li, Q.; Wang, J.; Xue, C.; Wang, S.; Yang, X.; Tian, G.; Su, H.; Li, X.; Miao, Y. Transforming detrimental intermetallics by accumulative thermal and strain energies in the Al–Fe–Si alloy. *J. Mater. Sci.* **2024**, *59*, 1699–1720. [CrossRef]

8.   Moore, E.; Turchi, P.; Lordi, V.; Weiss, D.; Sims, Z.; Henderson, H.; Kesler, M.; Rios, O.; McCall, S.; Perron, A. Thermodynamic Modeling of the Al-Ce-Cu-Mg-Si System and Its Application to Aluminum-Cerium Alloy Design. *J. Phase Equilibria Diffus.* **2020**, *41*, 764–783. [CrossRef]

9.   Liu, G.; Müller, D.B. Addressing sustainability in the aluminum industry: A critical review of life cycle assessments. *J. Clean. Prod.* **2012**, *35*, 108–117. [CrossRef]

10. Shabestari, S. The effect of iron and manganese on the formation of intermetallic compounds in aluminum–silicon alloys. *Mater. Sci. Eng. A* **2004**, *383*, 289–298. [CrossRef]

11. Wang, E.; Hui, X.; Chen, G. Eutectic Al–Si–Cu–Fe–Mn alloys with enhanced mechanical properties at room and elevated temperature. *Mater. Des.* **2011**, *32*, 4333–4340. [CrossRef]

12. Liu, C.; Garner, A.; Zhao, H.; Prangnell, P.B.; Gault, B.; Raabe, D.; Shanthraj, P. CALPHAD-informed phase-field modeling of grain boundary microchemistry and precipitation in Al-Zn-Mg-Cu alloys. *Acta Mater.* **2021**, *214*, 116966. [CrossRef]

13. Liu, C.; Davis, A.; Fellowes, J.; Prangnell, P.B.; Raabe, D.; Shanthraj, P. CALPHAD-informed phase-field model for two-sublattice phases based on chemical potentials: η-phase precipitation in Al-Zn-Mg-Cu alloys. *Acta Mater.* **2022**, *226*, 117602. [CrossRef]

14. Zhang, F.; Liang, S.; Zhang, C.; Chen, S.; Lv, D.; Cao, W.; Kou, S. Prediction of cracking susceptibility of commercial aluminum alloys during solidification. *Metals* **2021**, *11*, 1479. [CrossRef]

15. Jha, R.; Dulikravich, G.S. Temperature Regimes and Chemistry for Stabilizing Precipitation Hardening Phases in Al–Sc Alloys: Combined CALPHAD–Deep Machine Learning. *ASME Open J. Eng.* **2022**, *1*, 1–12. [CrossRef]

16. Jreidini, P.; Pinomaa, T.; Wiezorek, J.M.; McKeown, J.T.; Laukkanen, A.; Provatas, N. Orientation gradients in rapidly solidified pure aluminum thin films: Comparison of experiments and phase-field crystal simulations. *Phys. Rev. Lett.* **2021**, *127*, 205701. [CrossRef] [PubMed]

17. Chen, J.; Guo, M.; Yang, M.; Cui, T.; Cui, B.; Zhang, J. Insight into element segregation mechanisms during creep in γ'-strengthened Co-based superalloy by elastoplastic phase-field simulation. *Prog. Nat. Sci. Mater. Int.* **2024**, *34*, 873–879. [CrossRef]

18. Liu, X.; Shen, W.; Liu, W. Phase-Field Simulation of Precipitation and Grain Boundary Segregation in Fe-Cr-Al Alloys under Irradiation. *Nanomaterials* **2024**, *14*, 1198. [CrossRef] [PubMed]

19. Gong, T.Z.; Chen, Y.; Hao, W.Y.; Chen, X.Q.; Li, D.Z. Modeling segregation of Fe–C alloy in solidification by phase-field method coupled with thermodynamics. *Metals* **2023**, *13*, 1148. [CrossRef]

20. Staublin, P.; Mukherjee, A.; Warren, J.A.; Voorhees, P.W. Phase-field model for anisotropic grain growth. *Acta Mater.* **2022**, *237*, 118169. [CrossRef]

21. Steinbach, I. Phase-field models in materials science. *Model. Simul. Mater. Sci. Eng.* **2009**, *17*, 073001. [CrossRef]

22. Ji, Y.; Ghaffari, B.; Li, M.; Chen, L.Q. Phase-field modeling of θ' precipitation kinetics in 319 aluminum alloys. *Comput. Mater. Sci.* **2018**, *151*, 84–94. [CrossRef]

23. Provatas, N.; Elder, K. *Phase-Field Methods in Materials Science and Engineering*; John Wiley & Sons: Hoboken, NJ, USA, 2011.

24. Jokisaari, A.M.; Voorhees, P.W.; Guyer, J.E.; Warren, J.A.; Heinonen, O.G. Phase field benchmark problems for dendritic growth and linear elasticity. *Comput. Mater. Sci.* **2018**, *149*, 336–347. [CrossRef]

25. Biswas, S.; Schwen, D.; Singh, J.; Tomar, V. A study of the evolution of microstructure and consolidation kinetics during sintering using a phase field modeling based approach. *Extrem. Mech. Lett.* **2016**, *7*, 78–89. [CrossRef]

26. Biswas, S.; Schwen, D.; Tomar, V. Implementation of a phase field model for simulating evolution of two powder particles representing microstructural changes during sintering. *J. Mater. Sci.* **2018**, *53*, 5799–5825. [CrossRef]

27. Militzer, M. Phase field modeling of microstructure evolution in steels. *Curr. Opin. Solid State Mater. Sci.* **2011**, *15*, 106–115. [CrossRef]

28. Lacaze, J.; Eleno, L.; Sundman, B. Thermodynamic assessment of the aluminum corner of the Al-Fe-Mn-Si system. *Metall. Mater. Trans. A* **2010**, *41*, 2208–2215. [CrossRef]

29. Warmuzek, M.; Ratuszek, W.; Sęk-Sas, G. Chemical inhomogeneity of intermetallic phases precipitates formed during solidification of Al-Si alloys. *Mater. Charact.* **2005**, *54*, 31–40. [CrossRef]

30. Allen, C.; O'reilly, K.; Cantor, B.; Evans, P. Intermetallic phase selection in 1XXX Al alloys. *Prog. Mater. Sci.* **1998**, *43*, 89–170. [CrossRef]

31. Arbeiter, J.; Vončina, M.; Volšak, D.; Medved, J. Evolution of Fe-based intermetallic phases during homogenization of Al–Fe hypoeutectic alloy. *J. Therm. Anal. Calorim.* **2020**, *142*, 1693–1699. [CrossRef]

32. Wang, X.; Guan, R.; Misra, R.; Wang, Y.; Li, H.; Shang, Y. The mechanistic contribution of nanosized Al3Fe phase on the mechanical properties of Al-Fe alloy. *Mater. Sci. Eng. A* **2018**, *724*, 452–460. [CrossRef]

33. Ansara, I.; Dinsdale, A.; Rand, M. *Thermochemical Database for Light Metal Alloys*; Office for Official Publications of the European Communities: Luxembourg, 1998.

34. Eleno, L.; Vezelỳ, J.; Sundman, B.; Cieslar, M.; Lacaze, J. Assessment of the Al corner of the ternary Al–Fe–Si system. *Mater. Sci. Forum* **2010**, *649*, 523–528. [CrossRef]

35. Zakharov, A.; Guldin, I.; Arnold, A. Phase Diagram of the Al–Si–Fe–Mn System in the 10–14% Si, 0–3% Fe, and 0-4% Mn Concentration Ranges.(Translation). *Russ. Metall.* **1989**, 209–213.

36. Flores-V, A.; Sukiennik, M.; Castillejos-E, A.; Acosta-G, F.; Escobedo-B, J. A kinetic study on the nucleation and growth of the Al8FeMnSi2 intermetallic compound for aluminum scrap purification. *Intermetallics* **1998**, *6*, 217–227. [CrossRef]

37. Onderka, B.; Sukiennik, M.; Fitzner, K. Determination of the stability of Al11. 8FeMn1. 6Si1. 6 phase existing in the quaternary Al-Fe-Mn-Si system. *Arch. Metall.* **2000**, *45*, 119–132.

38. Munson, D. A clarification of the phases occurring in aluminium-rich aluminium-iron-silicon alloys, with particular reference to the ternary phase alpha-AlFeSi. *Inst. Met. J.* **1967**, *95*, 217–219.

39. Tibballs, J.; Horst, J.; Simensen, C. Precipitation of α-Al (Fe, Mn) Si from the melt. *J. Mater. Sci.* **2001**, *36*, 937–941. [CrossRef]

40. Steinbach, I.; Pezzolla, F.; Nestler, B.; Seeßelberg, M.; Prieler, R.; Schmitz, G.J.; Rezende, J.L. A phase field concept for multiphase systems. *Phys. D Nonlinear Phenom.* **1996**, *94*, 135–147. [CrossRef]

41. Uddagiri, M.; Shchyglo, O.; Steinbach, I.; Tegeler, M. Solidification of the Ni-based superalloy CMSX-4 simulated with full complexity in 3-dimensions. *Prog. Addit. Manuf.* **2023**, *9*, 1835–1841. [CrossRef]

42. Wang, Z.; Liang, C.; Wang, D.; Yue, X.; Li, J.; Ding, X. Unveiling the Co effect on the temporal evolution kinetics of γ' phase in Ni–Al–Co model superalloys via CALPHAD–informed phase field simulations. *Acta Mater.* **2023**, *258*, 119247. [CrossRef]

43. Wang, Z.; Liang, C.; Wang, D.; Ding, X. Uncovering the effect of Mo addition on the precipitation kinetics of the γ' phase in Ni–Al–Mo model superalloys using CALPHAD-assisted phase-field simulations. *J. Mater. Sci.* **2024**, *59*, 1–20. [CrossRef]

44. Thakur, A.K.; Kovacevic, S.; Manga, V.R.; Deymier, P.A.; Muralidharan, K. A first-principles and CALPHAD-assisted phase-field model for microstructure evolution: Application to Mo-V binary alloy systems. *Mater. Des.* **2023**, *235*, 112443. [CrossRef]

45. Warnken, N.; Ma, D.; Drevermann, A.; Reed, R.C.; Fries, S.; Steinbach, I. Phase-field modelling of as-cast microstructure evolution in nickel-based superalloys. *Acta Mater.* **2009**, *57*, 5862–5875. [CrossRef]

46. Steinbach, I.; Böttger, B.; Eiken, J.; Warnken, N.; Fries, S. CALPHAD and phase-field modeling: A successful liaison. *J. Phase Equilibria Diffus.* **2007**, *28*, 101–106. [CrossRef]

47. Keller, T.; Lindwall, G.; Ghosh, S.; Ma, L.; Lane, B.M.; Zhang, F.; Kattner, U.R.; Lass, E.A.; Heigel, J.C.; Idell, Y.; et al. Application of finite element, phase-field, and CALPHAD-based methods to additive manufacturing of Ni-based superalloys. *Acta Mater.* **2017**, *139*, 244–253. [CrossRef] [PubMed]

48. Tegeler, M.; Shchyglo, O.; Kamachali, R.D.; Monas, A.; Steinbach, I.; Sutmann, G. Parallel multiphase field simulations with OpenPhase. *Comput. Phys. Commun.* **2017**, *215*, 173–187. [CrossRef]

49. Greer, A. Overview: Application of heterogeneous nucleation in grain-refining of metals. *J. Chem. Phys.* **2016**, *145*, 211704. [CrossRef]

50. Uddagiri, M.; Shchyglo, O.; Steinbach, I.; Wahlmann, B.; Koerner, C. Phase-field study of the history-effect of remelted microstructures on nucleation during additive manufacturing of ni-based superalloys. *Metall. Mater. Trans. A* **2023**, *54*, 1825–1842. [CrossRef]

51. Park, J.; Oh, C.S.; Kang, J.H.; Jung, J.G.; Lee, J.M. Solidification and Precipitation Microstructure Simulation of a Hypereutectic Al–Mn–Fe–Si Alloy in Semi-Quantitative Phase-Field Modeling with Experimental Aid. *Metals* **2020**, *10*, 1325. [CrossRef]

52. Hallstedt, B.; Khvan, A.V.; Lindahl, B.B.; Selleby, M.; Liu, S. PrecHiMn-4—A thermodynamic database for high-Mn steels. *Calphad* **2017**, *56*, 49–57. [CrossRef]

53. Johannes, H.; Michael, K.; Philipp, S.; Britta, N. Applications of the phase-field method for the solidification of microstructures in multi-component systems. *J. Indian Inst. Sci.* **2016**, *96*, 235–256.

54. Thesis, D. Characterization of Equilibrium Phases in 8xxx Alloys for the Optimization of the Thermodynamic Database for MatCalc. Ph.D. Thesis, Technische Universität Wien, Vienna, Austria, 2022.

55. Que, Z.; Fang, C.; Mendis, C.L.; Wang, Y.; Fan, Z. Effects of Si solution in θ-Al13Fe4 on phase transformation between Fe-containing intermetallic compounds in Al alloys. *J. Alloys Compd.* **2023**, *932*, 167587. [CrossRef]

56. Yan, X.; Ding, L.; Chen, S.; Xie, F.; Chu, M.; Chang, Y.A. Predicting microstructure and microsegregation in multicomponent aluminum alloys. In *Essential Readings in Light Metals: Volume 3 Cast Shop for Aluminum Production*; Springer: Berlin/Heidelberg, Germany, 2016; pp. 512–518.